Electronic structure of PbTe near the band gap*

G. M. T. Foley† and D. N. Langenberg
Department of Physics and Laboratory for Research on the Structure of Matter, University of Pennsylvania, Philadelphia, Pennsylvania 19104
(Received 13 September 1976)

Existing experimental data for the electronic band parameters of the conduction and valence bands of PbTe are analyzed and compared using a multiband model electron dispersion relation. The model permits the identification of inconsistencies among the data and the derivation of an improved set of band parameters. Among the principal conclusions are (i) the most commonly used value of the transverse-conduction-band-edge effective mass is too large; (ii) the conduction- and valence-band mass anisotropy ratios vary only weakly with carrier concentration, in contradiction to much of the early data for p-PbTe; (iii) existing theoretical calculations of the far-band contributions to the conduction- and valence-band-edge effective masses are not in very good agreement with experiment.

I. INTRODUCTION

The electronic band structure of PbTe has been the object of experimental and theoretical investigations for many years.[1] A considerable body of experimental data now exists relating to band parameters near the fundamental energy gap. In many instances, however, these data are inconsistent. Moreover, they seem never to have been critically analyzed with the aid of a theoretical model of sufficient scope to permit identification of the probable nature and sources of these inconsistencies and the establishment of a set of "most likely" parameters. Consequently, even some of the most recent theoretical studies of the PbTe band structure[2,3] have incorporated experimental parameter values which, as we shall see, there is reason to mistrust. In this paper we attempt to rectify this unsatisfactory situation through an analysis of the available data on conduction-and valence-band effective-mass parameters in PbTe.

II. MULTIBAND MODEL

PbTe has a small (0.19 eV) direct gap at the L points of the Brillouin zone. The free carriers, whether electrons or holes, are degenerate in all available samples, with typical Fermi energies of several tens of millielectron volts. Because of the smallness of the gap, the electronic dispersion relation $E(\vec{p})$ is substantially nonparabolic at these energies, with the consequence that experimentally measured effective masses at the Fermi surface depend on the Fermi energy and hence on the carrier concentration. For low carrier concentrations, the Fermi surface consists of four (eight half) prolate spheroids centered at the L points with long axes parallel to ⟨111⟩ directions. At higher carrier concentrations, the Fermi surface becomes nonellipsoidal.

The energy levels at the L points in PbTe consist of the conduction- and valence-band edges, separated by 0.19 eV, two pairs of levels about 2 eV above and below the gap region, and remaining levels 10 eV or more away.[3] The dispersion relation which we shall use to describe the electronic structure near the band gap has been discussed and used by many workers.[2,4-6] It is obtained from a $\vec{k}\cdot\vec{p}$ perturbation calculation in which the interaction between the conduction- and valence-band-edge levels is treated exactly and interactions with other bands taken to second order. For present purposes, the dispersion relation for zero magnetic field and neglecting spin suffices. It is

$$\left(\frac{E_g}{2}-E+\frac{p_\perp^2}{2m_{tc}}+\frac{p_3^2}{2m_{lc}}\right)\left(\frac{-E_g}{2}-E-\frac{p_\perp^2}{2m_{tv}}-\frac{p_3^2}{2m_{lv}}\right)=\frac{1}{m_0^2}(P_\perp^2p_\perp^2+P_\parallel^2p_3^2). \quad (1)$$

Here the zero of energy E is at the midpoint of the gap, and E is measured positive upwards into the conduction band. E_g is the fundamental gap energy (positive), p_3 and $p_\perp$ are the components of crystal momentum parallel and perpendicular to a ⟨111⟩ direction, respectively, and m_0 is the free-electron mass. $P_\parallel$ and $P_\perp$ are the longitudinal and transverse momentum matrix elements taken between the conduction- and valence-band-edge states. The parameters m_{tc}, m_{lc}, m_{tv}, and m_{lv} represent contributions to the effective masses which result from interaction of the conduction- and valence-band-edge states with more distant bands. They are of the form

$$m_0/m_{tc}=1+M_{tc};\quad m_0/m_{lc}=1+M_{lc};\qquad m_0/m_{tv}=-1+M_{tv};\quad m_0/m_{lv}=-1+M_{lv}. \quad (2)$$

The M's are sums of terms of the form $\langle p\rangle^2/m_0\Delta E$,

where $\langle p \rangle$ is a momentum matrix element connecting a gap-edge state and one of the distant states, and ΔE is the appropriate energy denominator. Theoretical calculations of these far-band contributions usually include only the six levels nearest the gap region, including the conduction- and valence-band-edge levels. Hence the model is often called the "six-band model." Since these far-band mass parameters could include contributions from other bands as well, we shall refer to the model as the "multiband model" (MBM).

Equation (1) describes both the conduction and valence bands, and contains seven independent parameters which one might hope to obtain from experiment.

For comparison with experimental data, it is convenient to rewrite the MBM dispersion relation, Eq. (1). For the valence band, with energy now measured positive downwards from the band edge, the desired form is

$$E_v\left(1+\frac{E_v}{E_g}\right)=\frac{p_\perp^2}{2m_{1v}}\left(1+\frac{E_v}{E_g}\Delta_{1v}\right)+\frac{p_3^2}{2m_{3v}}\left(1+\frac{E_v}{E_g}\Delta_{3v}\right)+\frac{p_\perp^4}{4m_{1v}^2E_g}Q_{1v}+\frac{p_\perp^2p_3^2}{4m_{1v}m_{3v}E_g}Q_{2v}+\frac{p_3^4}{4m_{3v}^2E_g}Q_{3v}\,. \tag{3}$$

The new parameters which appear here are related to those which appear in Eq. (1) as follows: m_{1v} and m_{3v} are, respectively, the transverse and longitudinal effective masses at the valence-band-edge and are given by

$$\frac{m_0}{m_{1v}}=\frac{2P_\perp^2}{m_0E_g}+\frac{m_0}{m_{tv}};\quad \frac{m_0}{m_{3v}}=\frac{2P_\parallel^2}{m_0E_g}+\frac{m_0}{m_{lv}}\,. \tag{4}$$

Δ_{1v} and Δ_{3v} are measures of the *difference* between the conduction- and valence-band-edge masses, and hence the *asymmetry* between the two principal bands. They are given by

$$\Delta_{1v}=m_{1v}(m_{tv}^{-1}-m_{tc}^{-1})=1-m_{1v}/m_{1c}\,,\qquad \Delta_{3v}=m_{3v}(m_{lv}^{-1}-m_{lc}^{-1})=1-m_{3v}/m_{3c}\,. \tag{5}$$

Further,

$$Q_{1v}=\frac{m_{1v}^2}{m_{tc}m_{tv}};\quad Q_{2v}=m_{1v}m_{3v}\left(\frac{1}{m_{tc}m_{lv}}+\frac{1}{m_{tv}m_{lc}}\right);\quad Q_{3v}=m_{3v}^2/m_{lc}m_{lv}\,. \tag{6}$$

It should be noted that we have introduced one redundant parameter.

The dispersion relation for the conduction band, with energy measured positive upwards from the band edge, can be obtained from Eqs. (3)–(6) simply by interchanging the subscripts "c" and "v" everywhere. This introduces seven more redundant parameters. Some useful translation relations are

$$m_{1c}=m_{1v}/(1-\Delta_{1v});\quad m_{3c}=m_{3v}/(1-\Delta_{3v});\quad \Delta_{1c}=\Delta_{1v}/(\Delta_{1v}-1);\quad \Delta_{3c}=\Delta_{3v}/(\Delta_{3v}-1);\quad Q_{1c}=Q_{1v}/(1-\Delta_{1v})^2;\quad Q_{2c}=Q_{2v}/(1-\Delta_{1v})(1-\Delta_{3v});\quad Q_{3c}=Q_{3v}/(1-\Delta_{3v})^2. \tag{7}$$

Several comments on Eq. (3) are in order: (a) It is nonparabolic and describes nonellipsoidal energy surfaces. (b) If the terms quartic in p (the terms with Q factors) are dropped, it remains nonparabolic but the energy surfaces are then ellipsoidal. (c) This ellipsoidal but nonparabolic approximation depends *explicitly* on the deviation from mirror symmetry of the conduction and valence bands. It is often said that the conduction and valence bands of PbTe (and the other lead chalcogenides) are mirror images. This is approximately true, but not exactly so, and, as we shall see, the difference is important. (d) Two models commonly used to analyze experimental data for PbTe and similar materials are the (ellipsoidal nonparabolic) Kane model,[7] with dispersion relation

$$E(1+E/E_g)=p_\perp^2/2m_1+p_3^2/2m_3 \tag{8}$$

and the Cohen model[4] with (conduction band) dispersion relation

$$E_c=\frac{p_\perp^2}{2m_{1c}(1+E/E_g+p_3^2/2m_{3v}E_g)}+\frac{p_3^2}{2m_{3c}}, \tag{9}$$

with (nonellipsoidal nonparabolic) or without (ellipsoidal nonparabolic) the term containing m_{3v}. [Equation (9) is actually an approximation to a more general dispersion relation given by Cohen.[4]] The Kane model follows from Eq. (3) if we assume that m_{tc}, m_{lc}, m_{tv}, and m_{lv} are all infinite *or* drop terms quartic in p and assume $m_{tc}=m_{tv}$ and $m_{lc}=m_{lv}$. Either set of assumptions is equivalent to assuming exact mirror symmetry of the conduction and valence bands. Any use of the Kane model to describe PbTe therefore depends implicitly on this (unjustified) assumption.

The Cohen model follows from Eq. (3) if we assume m_{tc} and m_{tv} are both infinite and set $P_\parallel=0$. While complete mirror symmetry of the conduction and valence bands is not assumed, since m_{3c} and m_{3v} may still be different, the assumption $m_{1c}=m_{1v}$ inherent in this model is no more justified for PbTe than the assumptions leading to the Kane model.

We now proceed to consider some experimental data within the framework provided by the MBM. Expressions for various necessary experimentally measured quantities are derived in the Appendix.

III. ANALYSIS OF EXPERIMENTAL DATA

A. Dependence of transverse cyclotron masses on carrier concentration

The data points in Fig. 1 represent measured values of the transverse normalized (to the free-electron mass) cyclotron effective mass μ_{min} in p-PbTe as a function of the minimum de Haas–van Alphen frequency F_{min} (magnetic field parallel to a ⟨111⟩ axis). F_{min} is proportional to the extremal (maximum) p-space cross-sectional area of the Fermi surface in a plane normal to the magnetic field, and this area in turn depends on the Fermi energy and hence the carrier concentration. The strong nonparabolicity of the valence band in PbTe is manifest in the dependence of the cyclotron mass on de Haas–van Alphen frequency.

We have plotted μ^2_{min} rather than μ_{min} because the Kane and Cohen models both yield a simple linear relation between μ^2_{min} and F_{min},

$$\mu^2_{min} = (m_1/m_0)^2[1 + 4(F_{min} m_0/F_0 m_1)], \qquad (10)$$

where $F_0 = m_0 c E_g/e\hbar$. We might expect the corresponding relation for the MBM to be rather similar.

With the exception of one point, all the data in Fig. 1 were derived from simultaneous measurements of cyclotron masses and de Haas–van Alphen frequencies in some type of quantum-oscillation experiment, usually a Schubnikov–de Haas experiment.[8-11] The exception is from our own Faraday-mode cyclotron resonance experiments.[12] Effective masses derived from cyclotron resonance experiments are generally subject to uncertainties owing to the presence of nonlocal effects and, in the present instance, either from a need for extrapolation of measured masses to the band edge, or the establishment of a proper connection between the carrier concentration and de Haas–van Alphen frequency. For these reasons, the cyclotron resonance results of Nii[13] and Perkowitz[14] for p-PbTe have been omitted from Fig. 1. Our experiments were done on epitaxial films with sufficiently small carrier concentration ($\sim 5 \times 10^{16}$ cm^{-3}) that extrapolation to the band edge involved a negligible correction. Furthermore, the correction for nonlocal effects (proportional to $n^{5/9}\omega^{-2/3}$, where n is the carrier concentration and ω is the experimental frequency), was very small (~3%) because of the low carrier concentration and relatively high frequencies (140 and 330 GHz) used in our experiments.

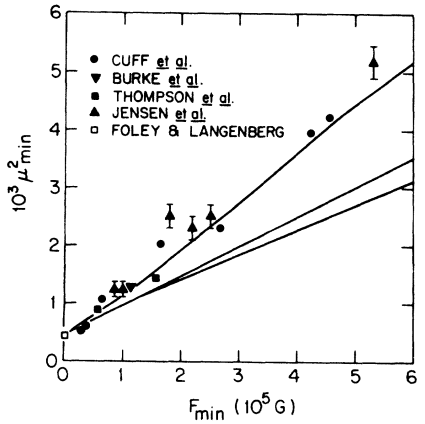

FIG. 1. Square of the normalized minimum cyclotron effective mass vs minimum de Haas–van Alphen frequency for p-PbTe. Sources of experimental data are Refs. 8–12. Curves are explained in the text.

The most commonly used experimental values of band edge effective masses in PbTe are those of Cuff *et al.*[8] They are $m_{1c}/m_0 = 0.024 \pm 0.003$ and $m_{1v}/m_0 = 0.022 \pm 0.003$. They were obtained by fitting data like those in Fig. 1 (the Cuff *et al.* data for p-PbTe are included in Fig. 1) with the equivalent of Eq. (10) derived from Eq. (3) with $m_{tc}/m_0 = 1$, $m_{tv}/m_0 = -1$ (all $M = 0$). Thompson *et al.*[10] later fitted their own data plus the Cuff *et al.* data with Eq. (10) and found $m_{1v}/m_0 = 0.018 \pm 0.003$. In both cases E_g was treated as an adjustable parameter and found to be substantially less than the known gap energy (see below) and, in the Cuff *et al.* case, slightly different for the conduction- and valence-band data. The source of this rather unsatisfactory situation lies in the neglect of the far-band contributions to the effective masses. The "gap energies" obtained in such fits are phenomenological "interaction gaps." The degree to which they differ from the measured optical gap reflects the importance of the far-band contributions to the effective masses and emphasizes the unsatisfactory nature of the approximations which yield these interaction gaps.

We have fitted the data of Fig. 1 using the full MBM as embodied in Eqs. (A15) and (A20) of the Appendix. In doing so, we fixed E_g at the measured direct gap. This has been determined in two different experiments. Mitchell *et al.*[15] found $E_g = 0.190 \pm 0.002$ eV from magneto-optical studies of epitaxial films, and Butler and Calawa[16] found $E_g = 0.187$ eV from magnetoemission studies with PbTe diode lasers. (Both results are for $T \to 0$ K.) These two results are in excellent agreement. We somewhat arbitrarily selected the latter, feeling that it is likely to be somewhat more accurate than the former. We then least-squares fitted various subsets of the data, with m_{1v}, Δ_{1v}, and Q_{1v} as adjustable parameters. Our results can be summarized as follows.

Although all of the data shown in Fig. 1 are fairly consistent, we believe the data of Burke *et al.*[9] and

Jensen *et al.*[11] are likely to be the most reliable of the quantum-oscillation data. In these experiments, in contrast to the others, the de Haas–van Alphen frequencies were obtained from Fourier analysis of the raw data, complete angular dependences were measured, and good agreement was obtained between carrier concentrations determined from quantum oscillation data and from Hall measurements. We have therefore concentrated our fitting on these data plus our own cyclotron-resonance datum. A weighted least-squares fit to this subset of data gave a minimum χ^2 of about 10, substantially larger than the expected value (the number of degrees of freedom) of 4. Deletion of the rather divergent Jensen *et al.* point at $F_{\min} = 1.8 \times 10^5$ G reduced the minimum χ^2 to 1.0, much less than the expected value of three, indicating a very good fit. The fitted valence-band-edge mass is $m_{1v}/m_0 = 0.0210 \pm 0.0008$. (The uncertainties quoted here and in the following are intended as one-standard-deviation uncertainties.) The values of Δ_{1v} and Q_{1v} corresponding to the minimum χ^2 are $\Delta_{1v} = -0.47$ and $Q_{1v} = 0.09$. However, the fit was relatively insensitive to individual variation of Δ_{1v} and Q_{1v}. It appeared instead to depend primarily on their sum. The reason for this is evident from Eq. (A27); to first order and, very nearly, to second order as well, Δ_{1v} and Q_{1v} enter into the dependence of $\mu^2_{\min}$ on $F_{\min}$ only as the sum $\Delta_{1v} + Q_{1v}$. The two parameters become distinguishable only through the higher-order terms. Since we question whether the data of Fig. 1 are really adequate to discriminate reliably between Δ_{1v} and Q_{1v}, it seems to us more appropriate to consider the minimization of χ^2 with respect to the sum $\Delta_{1v} + Q_{1v}$ and to quote the result of the fit as $\Delta_{1v} + Q_{1v} = -0.38 \pm 0.10$.

The consistency of all the data in Fig. 1 is evidenced by the fact that a fit to the entire set (unweighted, because experimental uncertainties were not reported for some of the data) gave values of m_{1v} and $\Delta_{1v} + Q_{1v}$ which do not differ significantly from those given above.

The solid lines in Fig. 1, reading from top to bottom, correspond to Eqs. (A15) and (A20) with the final parameters recommended here (see Table II), Eq. (10) (the Kane and Cohen models) with $m_{1v}/m_0 = 0.021$ and $E_g = 0.187$ eV, and the model and parameters of Cuff *et al.*, except that we have used the measured gap, $E_g = 0.187$ eV, instead of their fitted "effective gap". The latter two curves are clearly rather poor fits to the data. The first is much better, although it is not the best-fit curve for these data alone because our final recommended parameters based on the totality of the data differ slightly from those derived from these data alone.

Having determined the transverse-valence-band parameters to the extent permitted by the available data, we consider the transverse-conduction-band-edge mass. We begin by noting that if the valence-band data yielded an unambiguous determination of m_{1v} and Δ_{1v}, m_{1c} could be inferred from these data alone without any reference to conduction-band data! As it is, we can only limit the range of likely values of m_{1c}. If we were to take seriously our fitted $\Delta_{1v} = -0.47$, it would imply $m_{1c}/m_0 = 0.0143$. A firmer inference can be drawn using the equations relating M_{tc} and M_{tv} to the fitting parameters:

$$M_{tc} = -\left(1 + \frac{\Delta_{1v}}{2}\frac{m_0}{m_{1v}}\right) \pm \frac{1}{2}\frac{m_0}{m_{1v}}(\Delta_{1v}^2 + 4Q_{1v})^{1/2},$$
$$M_{tv} = \left(1 + \frac{\Delta_{1v}}{2}\frac{m_0}{m_{1v}}\right) \pm \frac{1}{2}\frac{m_0}{m_{1v}}(\Delta_{1v}^2 + 4Q_{1v})^{1/2}, \tag{11}$$

where the upper signs or the lower signs are to be taken together. Given the constraints that the M's must be real (so that $\Delta_{1v}^2 + 4Q_{1v} \geq 0$) and $\Delta_{1v} + Q_{1v} = -0.38 \pm 0.10$, Δ_{1v} *cannot* be algebraically greater than -0.35 ± 0.09 for *any* value of Q_{1v} (disregarding unphysically large values)! This implies that m_{1c}/m_0 can be no larger than 0.0156 ± 0.0012.

Turning to experimental information on m_{1c}, we find that the range of values inferred above from the valence-band data lies substantially below all but one of the reported experimental values. These are summarized in Table I. The one exception is our own cyclotron resonance result.[12] (This unexpectedly low value provided the original impetus for the data analysis reported in this paper.) We are at a loss to account for the generally high values previously reported except to note that in the microwave-frequency cyclotron-resonance work of Nii and Numata and Uemura[13] and Fujimoto,[17] corrections for nonlocal effects were not made. Such a correction would lower their values of m_{1c}. Nonlocal effects were explicitly treated by Walpole and McWhorter[18] and their value of m_{1c} is the lowest among those previously reported.

The valence-band data leave little room for doubt that the transverse-conduction-band-edge mass must be less than the transverse-valence-band-edge mass by several tens of percent despite indications to the contrary from almost all existing conduction-band data. On the basis of the foregoing discussion, we have elected to use our own experimental value, $m_{1c}/m_0 = 0.0164 \pm 0.001$, as the best available estimate of m_{1c}. Taken together with our fitted value of m_{1v}, it implies $\Delta_{1v} = -0.28 \pm 0.09$.

The implications of these conclusions for the far-band contributions to the transverse masses are presented in Fig. 2. The curved shaded band covers the values of M_{tc} and M_{tv} allowed by the constraint derived from our fit to the valence-band data, $\Delta_{1v} + Q_{1v} = -0.38 \pm 0.10$. The straight shaded band covers the values allowed if instead we use our recommended values of m_{1c} and m_{1v}. It is sim-

TABLE I. Experimental values of transverse-conduction-band-edge mass. Extrapolated band edge values were reported by Cuff *et al.* and by Walpole and McWhorter. In the other cases, the extrapolation was made by us using the MBM model with parameters derived in the present paper. This extrapolation typically lowered the originally reported values by 5–20%.

Reference	m_{1c}/m_0	Experiment
8	0.024 ± 0.003	from model fit to Schubnikov–de Haas data; data not reported
13	0.022	cyclotron resonance
17	0.021	cyclotron resonance
18	0.020	helicon propagation
14	0.035	cyclotron resonance
19	0.022	ir magnetoreflectivity
20	0.023	ir magnetoreflectivity
12	0.0164 ± 0.001	cyclotron resonance

ply a plot of the relation

$$M_{tv} - M_{tc} = 2 + m_0/m_{1v} - m_0/m_{1c}, \qquad (12)$$

which is easily derivable from Eqs. (2) and (4). The straight unshaded band corresponds to the band-edge masses of Cuff *et al.*[8] The difference between the two straight bands results mainly from the difference between the experimental transverse-conduction-band-edge mass of Cuff *et al.* (which is typical of most of those in Table I) and ours. We see that the latter is consistent with the result of our fit to the valence-band data whereas the former clearly is not.

Note that, although the data determine the difference $M_{tv} - M_{tc}$ [Eq. (12)] with some reliability, they impose only the loosest of limits on the possible individual values of M_{tc} and M_{tv}. Their determination would require accurate determination of Q_{1v}, i.e., of the nonellipsoidal distortion of the Fermi surface. The location of the double-shaded overlap region in Fig. 2 suggests only that Q_{1v} probably lies somewhere in the range -0.03 to 0.14. The points and error bars on the central line of the straight shaded band are derived from the value of Q_{1v} and its uncertainty obtained from the fitting procedure of Sec. III B.

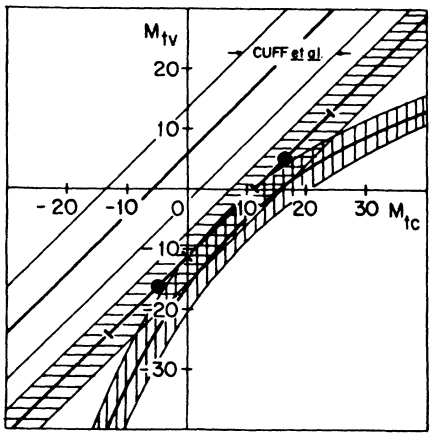

FIG. 2. Far-band contributions to the transverse effective masses. Bands indicate ranges of values of M_{tc} and M_{tv} consistent with various experimental data. For detailed discussion see text.

Theoretically calculated values of M_{tc} and M_{tv} are generally nearly equal to magnitude, have positive signs, and lie in the range 5–8.[21,22] It is clear from Fig. 2 that these theoretical results are inconsistent with the experimental data, which indicate that M_{tc} and M_{tv} should be in or near the overlap region of the two shaded bands. The generally accepted parity assignments[3] for the energy levels near the gap require that M_{tv} and M_{tc} both have positive signs. Even the inversion of the L_6^+ and L_6^- levels at the gap would leave these signs unchanged. For M_{tc} and M_{tv} both positive, the experimental data indicate that M_{tc} must be substantially larger than M_{tv} (perhaps a factor of 3 or more). Recent suggestions[23,24] of a more dramatic change in parity assignments would imply negative signs for both M_{tc} and M_{tc}. If this were so, we would draw the opposite conclusion about the magnitudes of M_{tc} and M_{tv} from Fig. 2.

B. Dependence of mass anisotropy ratios on carrier concentration

Experimental data which relate to the longitudinal band parameters in PbTe have generally been reported in terms of the so-called mass-anisotropy ratio K. For a spheroidal parabolic band with transverse and longitudinal effective masses m_1 and m_3, $K \equiv m_3/m_1$. For a nonparabolic and possibly nonellipsoidal band, some care is required in the definition and use of K, as discussed in the Appendix. Two different K's may be defined in terms of experimental quantities, one in terms of the maximum and minimum de Haas–van Alphen

frequencies, $K_q \equiv (F_{max}/F_{min})^2$, and the other in terms of the maximum and minimum cyclotron masses, $K_\mu \equiv (\mu_{max}/\mu_{min})^2$. Both depend on the Fermi energy and hence the carrier concentration. We now consider the available experimental data for K_q and K_μ as a function of carrier concentration.

The data are shown in Fig. 3. Consider first the data for p-PbTe, Fig. 3(b). It happens that most of these data are from quantum-oscillation experiments (solid symbols), so K_{qv} is the relevant K. Most of the data fall into two groups: The first group, including the vanguard data of Cuff *et al.*,[8,25] indicates that K_{qv} decreases from about 14 at the band edge to about six at a carrier concentration of 3×10^{18} cm^{-3}. The other, containing data of Schilz,[26] Burke *et al.*,[9] and Jensen *et al.*[11] (excluding the one high Schilz point at 5.4×10^{18} cm^{-3}) indicates that K_{qv} varies much more slowly with carrier concentration. The two groups are clearly inconsistent.

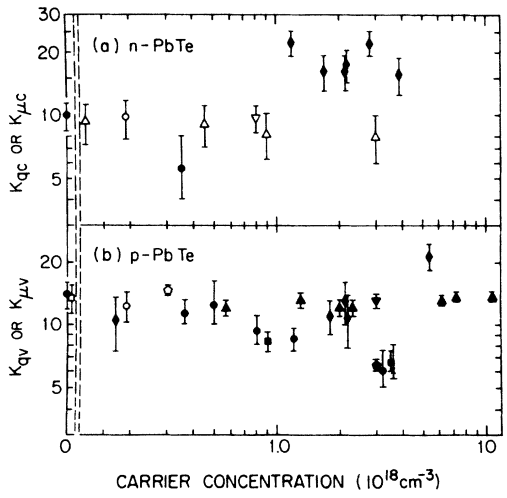

FIG. 3. Mass anisotropy ratio vs carrier concentration for (a) n-PbTe and (b) p-PbTe. Solid symbols represent data from quantum oscillation experiments and correspond to K_{qc} or K_{qv}. Open symbols represent data from cyclotron resonance experiments and correspond to $K_{\mu c}$ or $K_{\mu v}$. Sources of experimental data are: (●) Cuff *et al.* (Refs. 8 and 25); (○) Nii, Numata, and Uemura (Ref. 13); (▽) Perkowitz (Ref. 14); (△) Fujimoto (Ref. 17); (♦) Schilz (Ref. 26); (▼) Burke *et al.* (Ref. 9); (■) Thompson *et al.* (Ref. 10); (▲) Jensen *et al.* (Ref. 11); (□) Foley and Langenberg (Ref. 12); (◊ ♦) Stiles *et al.* (Refs. 27 and 28); (×) Coste (Ref. 29). K values not directly quoted by the original authors were derived by us from the reported data. Uncertainties in K not directly quoted by the original authors were estimated by us from the scatter in the reported data. K's to the left of the break in the logarithmic scale are band edge values reported by the indicated authors.

We may judge which group is likely to be more reliable using the MBM model. Consider Eq. (A28). At a carrier concentration of 3×10^{18} cm^{-3}, $(N_v/N_{0v})^{2/3}$ is about $\frac{1}{3}$, so the first three terms of this series should suffice for qualitative argument. The difference $\Delta_{1v}-\Delta_{3v}$ can be written

$$\Delta_{1v}-\Delta_{3v}=(1-\Delta_{1v})(K_{0v}/K_{0c}-1). \tag{13}$$

We have seen that $1-\Delta_{1v}$ is about 1.3. All the data of Fig. 3 suggest rather strongly that K_{0v}/K_{0c} is larger than 1 and is probably in the range 1.2–1.4. We thus expect $\Delta_{1v}-\Delta_{3v}$ to be positive and to lie in the range 0.2–0.5. It is then clear from Eq. (A28) that, if K_{qv} actually decreases (the first group of data) or increases (the one high Schilz point) by something like a factor of 2 between the band edge and a carrier concentration of (3–6) $\times10^{18}$ cm^{-3}, the Q's must be on the order of one or larger. This would imply nonellipsoidal distortions of the Fermi surface much larger than are generally observed (and would invalidate the basis for the MBM model, the assumption that the far-band contributions to the band edge masses are relatively small compared with the contribution of the direct conduction–valence-band interaction). We conclude that the data of the first group, although internally consistent, are simply unreliable, and eliminate them from further consideration. We have deleted the one high Schilz value for the same reason and have also elected to delete the remainder of the Schilz data because their experimental uncertainties are relatively large and because the totality of the Schilz data for both n-PbTe and p-PbTe does not inspire confidence. For p-PbTe, we are thus left with the data of Burke *et al.* and Jensen *et al.*

Turning now to the data for n-PbTe [Fig. 3(a)], we note that they are rather sparse compared with those for p-PbTe. We eliminate at the outset the Schilz data because here again they would require an unlikely increase of K_{qc} by a factor of 2 above the band edge value. The remaining data appear rather consistent. Nevertheless, we have chosen to delete also the Cuff *et al.*[25] and Perkowitz[14] points, mainly because they come from experiments which yielded the highest values of m_{1c}, which we have seen above are unlikely to be reliable. The remaining data are all from cyclotron resonance experiments and are therefore subject to uncertainties owing to uncorrected nonlocal effects. However, nonlocal effects should partially cancel out of the *ratio* $K_{\mu c}=(\mu_{max}/\mu_{min})^2$. Furthermore, a fit to these data should give a reasonably good estimate of K_{0c} in the zero-carrier-concentration limit where nonlocal effects vanish, although the apparent variation of $K_{\mu c}$ with carrier concentration may be distorted by nonlocal effects. We

have therefore chosen to include these data in our basic data set.

We have carried out a four-parameter weighted least-squares fit to this selected set of data using Eqs. (A21), (A22), and (A26). E_g, m_{1v}, m_{1c}, and hence, Δ_{1v} were fixed at the values established in Sec. III A and K_{0v}, K_{0c}, Q_{1v}, and Q_{3v} were varied for best fit. A choice of K_{0v} and K_{0c} determined Δ_{3v} through Eq. (13), and a choice of Q_{1v} and Q_{3v} then determined Q_{2v} through

$$Q_{2v}=\tfrac{1}{2}\{-\Delta_{1v}\Delta_{3v}+[(\Delta_{1v}^2+4Q_{1v})(\Delta_{3v}^2+4Q_{3v})]^{1/2}\}. \quad (14)$$

The necessary conduction-band parameters were determined using the translation relations [Eq. (7)]. The resulting best-fit parameters are $K_{0c}=9.2\pm0.3$, $K_{0v}=11.6\pm0.2$, $Q_{1v}=0.03\pm0.10$, and $Q_{3v}=0.06\pm0.06$. The corresponding minimum χ^2 is 2.0 for nine degrees of freedom, indicating a considerably better fit than might be expected from the experimental uncertainties. Our selected set of K data are replotted in Fig. 4, using linear scales, together with best-fit curves calculated from our final recommended parameters and Eqs. (A21), (A22), and (A26).

The data of Jensen *et al.*[11] for K_{qv} appear to show a slight trend upward with increasing carrier concentration. It is clear from Eq. (13), the associated discussion, and Eq. (A28) that this is just what we would expect from the MBM and our fitted parameters. Jensen *et al.* chose to ignore this upward trend and to characterize their results by a carrier-concentration-independent $K_{qv}=13.0\pm0.5$. In order to test the validity of this conclusion, we have fitted a constant K_{qv} to the Burke *et al.* and Jensen *et al.* data. The resulting minimum χ^2 is 4.9 (at $K_{qv}=13.1$), for seven degrees of freedom, indicating a rather good fit. However, the contribution of these data to the minimum total χ^2 in our overall fit is only 1.8. We conclude, therefore, that the MBM with its carrier-concentration-dependent K_{qv} gives a significantly better fit to these data than a constant K_{qv} and that the upward trend in the experimental K_{qv} data is probably real. We note that a corresponding downward trend may be present in the $K_{\mu c}$ data. This is precisely consistent with the K_{qv} data: if K_{qv} increases with increasing carrier concentration and $\Delta_{1v}-\Delta_{3v}$ is therefore positive, then $\Delta_{1c}-\Delta_{3c}$ must be negative and, from Eq. (A29), $K_{\mu c}$ must decrease with increasing carrier concentration.

The Q_{1v} derived from this fit to the mass-anisotropy data is very consistent with the conclusions drawn from the transverse data in Sec. III A. Figure 5 is the analog of Fig. 2 for the longitudinal far-band mass parameters. The shaded band covers the values of M_{lv} and M_{lc} allowed by our derived value of Δ_{3v}. The points and error bars on the central line of the band indicate the M_{lc} and M_{lv} determined by the fitted value of Q_{3v}. The data place rather tighter constraints on the possible values of M_{lc} and M_{lv} than they do for M_{tc} and M_{tv}. M_{lc} and M_{lv} appear to be about an order of magnitude less than M_{tc} and M_{tv} and are more nearly equal in magnitude. Theoretical values of M_{lc} and M_{lv} are about 0.6–1.0 and 0.8–1.6, respectively.[21,22] These are not grossly inconsistent with the data, although the data suggest that M_{lc} is larger than M_{lv} rather than vice versa.

In Table II we summarize the results of our fits to the experimental data. The uncertainties assigned to the derived parameters have been estimated on the assumption that the uncertainties of the basic experimental or fitted parameters are uncorrelated. A study of the details of the fits indicates that this is not strictly true, but we do not believe that the errors introduced by this assumption are significant. The lower limit of the uncertainty for Q_{1v} has been truncated in accord

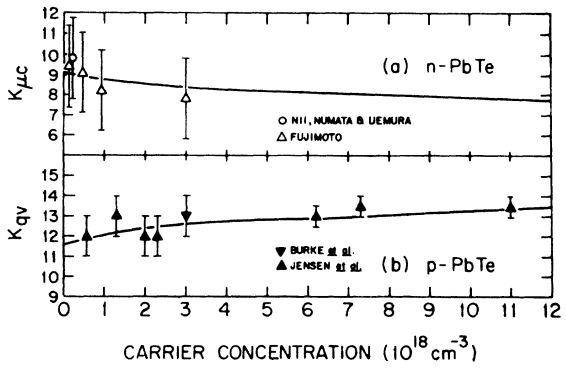

FIG. 4. Basic selected set of mass-anisotropy-ratio data from Fig. 3 and best-fit curves.

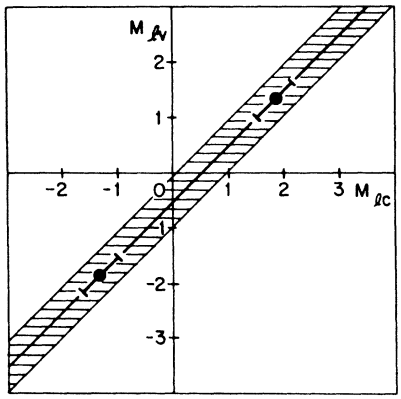

FIG. 5. Far-band contributions to the longitudinal effective masses. Shaded band indicates the range of values of M_{lc} and M_{lv} consistent with experimental data. For detailed discussion see text.

TABLE II. Final recommended parameters obtained by fitting the multiband model to experimental PbTe data.

	Conduction band	Valence band
	(a) Basic experimental or fitted parameters	
E_g (eV)	0.187	
m_1/m_0	0.0164 ± 0.001	0.0210 ± 0.0008
K_0	9.2 ± 0.3	11.6 ± 0.2
Q_1		$0.03^{+0.10}_{-0.04}$
Q_3		0.06 ± 0.06
	(b) Derived parameters	
m_3/m_0	0.151 ± 0.010	0.244 ± 0.010
Δ_1	0.22 ± 0.09	-0.28 ± 0.09
Δ_3	0.38 ± 0.13	-0.61 ± 0.13
Q_1	$0.02^{+0.06}_{-0.03}$	
Q_2	$0.04^{+0.06}_{-0.04}$	$0.09^{+0.13}_{-0.09}$
Q_3	0.02 ± 0.02	
F_0 (G)	1.62×10^7	
N_0 (cm^{-3})	$(9.36 \pm 0.06) \times 10^{18}$	$(1.52 \pm 0.07) \times 10^{19}$

with the theoretical expectation that, whatever the correct parity assignments for the energy levels at L may turn out to be, M_{tc} and M_{tv} must have the same sign.

In Figs. 6–12, we show the dependence of various quantities of interest on Fermi energy for both n-PbTe and p-PbTe. These have been calculated from the parameters of Table II and the appropriate equations from the Appendix. In each case the dashed line corresponds to the ellip-

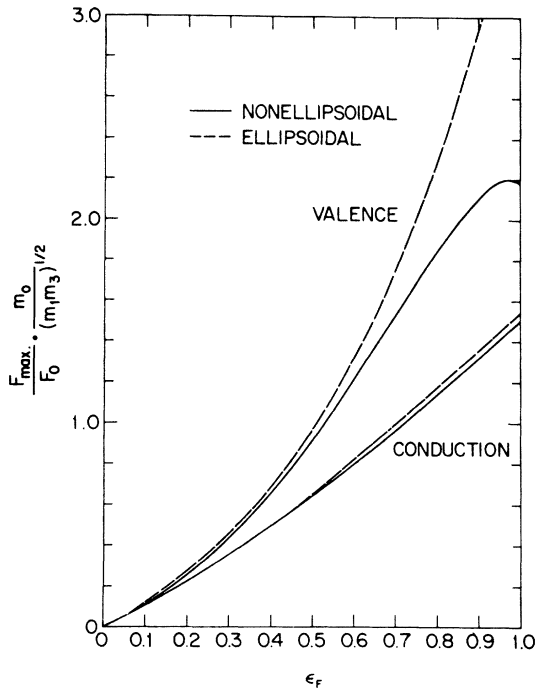

FIG. 6. Normalized maximum de Haas–van Alphen frequency vs Fermi energy for the multiband model with our recommended parameters. In a simple ellipsoidal parabolic model these curves would be a straight line with slope 1. $\epsilon_F \equiv E_F/E_g$.

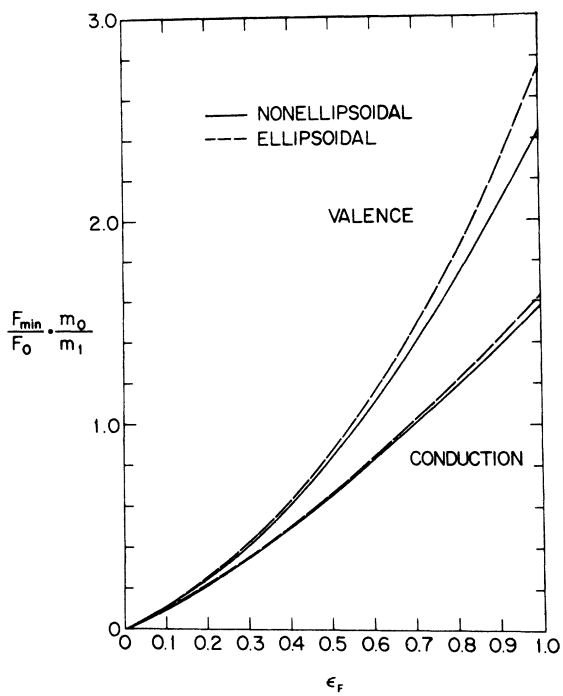

FIG. 7. Normalized minimum de Haas-van Alphen frequency vs Fermi energy for the multiband model with our recommended parameters. In a simple ellipsoidal parabolic model these curves would be a straight line with slope 1. $\epsilon_F \equiv E_F/E_g$.

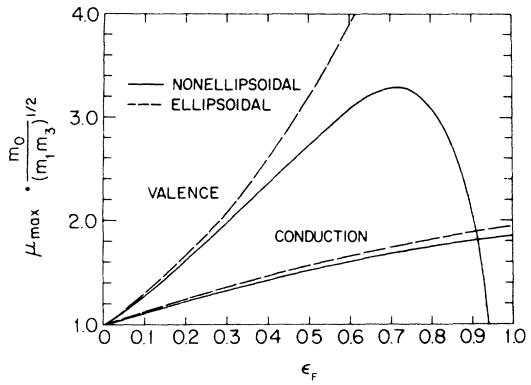

FIG. 8. Normalized maximum cyclotron mass vs Fermi energy for the multiband model with our recommended parameters. In a simple ellipsoidal parabolic model these curves would be a horizontal straight line on the bottom edge of the figure. $\epsilon_F \equiv E_F/E_g$.

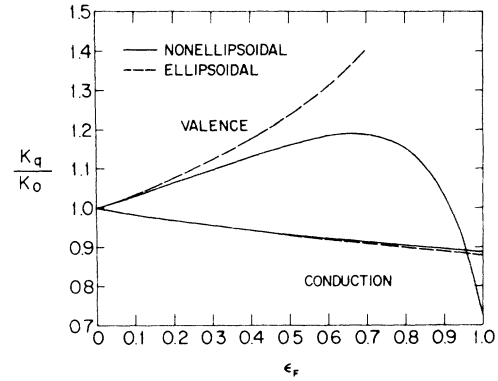

FIG. 10. Normalized quantum-oscillation mass anisotropy ratio vs Fermi energy for the multiband model with our recommended parameters. In a simple ellipsoidal parabolic model these curves would be the horizontal straight line $K_q/K_0 = 1$. $\epsilon_F \equiv E_F/E_g$.

soidal truncation of the MBM obtained by setting all Q's equal to zero, and the solid line shows the effect of including the Q terms. For F_{min} and μ_{min} the exact Eqs. (A15) and (A20) were used. For all other quantities we used the equations given in the Appendix which describe the nonellipsoidal perturbations only to first order in the Q's. Nonellipsoidal perturbations are clearly considerably more important in the valence band than in the conduction band. For the valence band, our expansion of the nonellipsoidal effects to first order in the Q's apparently fails at Fermi energies substantially less than the gap energy.

C. Nonellipsoidal distortions of the Fermi surface

We have seen that experimental data provide some evidence for rather small deviations from spheroidal shape of the Fermi surface in PbTe. In this section we comment further on this point.

Consider first the data of Jensen *et al.*,[11] upon which we have relied so heavily. Figure 13 is an adaptation of Fig. 4 in Ref. 11. It shows the measured F_{min} as a function of carrier concentration. All of these data points have been used in the foregoing analysis with the exception of that at the highest concentration (4.5×10^{19} cm^{-3}) which was omitted in the K analysis since no corresponding anisotropy ratio was reported. The dashed straight line with a slope of $\frac{2}{3}$ indicates the dependence expected from a simple ellipsoidal model with a carrier-concentration-independent $K_{qv} = 13$.[11] The deviation of the high-carrier-concentration point from this line was interpreted by Jensen *et al.* as evidence for the appearance of significant nonellipsoidal behavior at carrier concentrations above 10^{19} cm^{-3}.

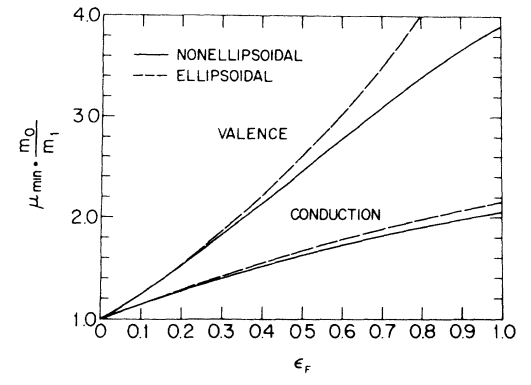

FIG. 9. Normalized minimum cyclotron mass vs Fermi energy for the multiband model with our recommended parameters. In a simple ellipsoidal parabolic model these curves would be a horizontal straight line on the bottom edge of the figure. $\epsilon_F \equiv E_F/E_g$.

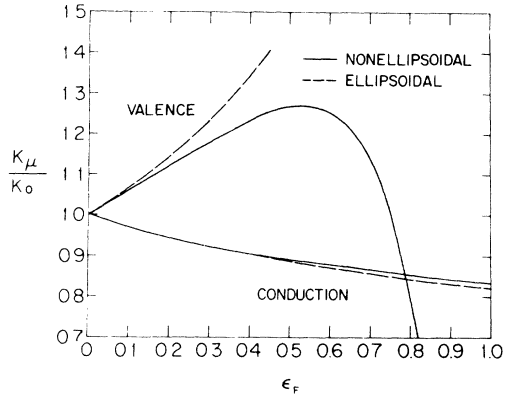

FIG. 11. Normalized cyclotron-mass anisotropy ratio vs Fermi energy for the multiband model with our recommended parameters. In a simple ellipsoidal parabolic model these curves would be the horizontal straight line $K_\mu/K_0 = 1$. $\epsilon_F \equiv E_F/E_g$.

We have calculated $F_{\min}$ vs N from Eqs. (A14) and (A26) using our fitted parameters (Table II). The resulting curve is virtually indistinguishable from the dashed straight line over the entire range of carrier concentrations shown in Fig. 13 and has therefore not been separately shown. At the lower carrier concentrations its slope is slightly less than $\frac{2}{3}$; this is essentially a consequence of the slight increase of K_{qv} with increasing carrier concentration. [Note that this occurs even in the ellipsoidal truncation ($Q_{1v}=Q_{2v}=Q_{3v}=0$) of the MBM.] At high carrier concentrations the curve tends to turn *up*, not down! The reason for this is suggested by the series expansion Eq. (A30): It is due to the growing importance of the nonellipsoidal terms at high carrier concentrations and the fact that our fitted Q's lead to *upward* deviations from the ellipsoidal truncation of the MBM. The ellipsoidal truncation actually gives a slightly better fit to the one high-carrier-concentration point. However, shifts of the Q's from our fitted values in the direction suggested by Eq. (A30) give a better fit yet. The solid line in Fig. 13 shows the result of using a Q_{1v} at the upper limit of its uncertainty range ($Q_{1v}=0.13$), a Q_{3v} at the lower limit of its uncertainty range ($Q_{3v}=0$), and the implied value for Q_{2v}, with all other parameters held fixed. We see that the Jensen *et al.* high-carrier-concentration point suggests that Q_{1v} and Q_{3v} are, respectively, larger and smaller than our fitted values, but within the uncertainties we have assigned them. [This should be borne in mind in considering the implications of the data for the far-band mass contributions (Figs. 2 and 5) and in comparing these with the results of theoretical calculations of these quantities.] We feel that the use of this one high-concentration datum to provide a yes or no judgment of the existence of significant nonellipsoidal behavior is thus somewhat dubious, but it is quite consistent with our analysis of all the other data.

Consider now the results of Schilz.[26] Schilz's results for the angular variation of the de Haas–van Alphen frequency in both n-PbTe and p-PbTe (Fig. 14) show extremely strong deviations from ellipsoidal behavior at carrier concentrations above about 2×10^{18} cm^{-3}. For comparison we show in the upper part of Fig. 14 the angular variation calculated from Eq. (A11) for p-PbTe at a carrier concentration of 5.4×10^{18} cm^{-3}. (Note that this is not a cross-section of the Fermi surface!) The dashed line represents the ellipsoidal prefactor in Eq. (A11). The solid line on the left was calculated using our fitted parameters. The nonellipsoidal distortion is of the same form as that observed by Schilz: $U_{\min}$ remains essentially constant at 0.018 from $\theta=0$ to $\theta\cong60°$, then increases rapidly to 0.032 at $\theta=90°$. The result is a tendency toward a squaring off of the end of the Fermi surface like that observed by Schilz. However, the size of the distortion is much smaller. The distortion can be made to look a little more like Schilz's by shifting the Q's. On the right we show the result of setting Q_{1v} near the lower limit of its uncertainty ($Q_{1v}=0$) and Q_{3v} at the upper limit of its uncertainty ($Q_{3v}=0.12$). (Note that this is the opposite of the Q-shift required to fit the Jensen

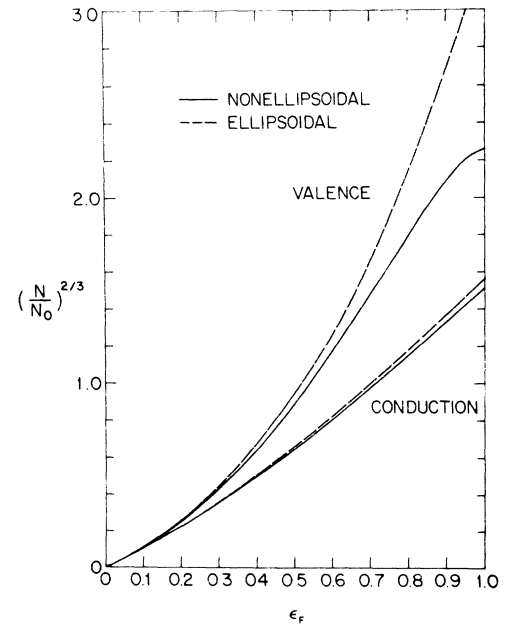

FIG. 12. (Normalized carrier concentration)$^{2/3}$ vs Fermi energy for the multiband model with our recommended parameters. In a simple ellipsoidal parabolic model these curves would be a straight line with slope 1. $\epsilon_F \equiv E_F/E_g$.

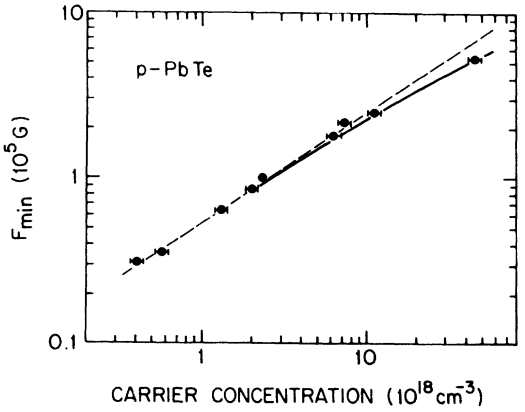

FIG. 13. Minimum de Haas-van Alphen frequency vs carrier concentration from the data of Burke *et al.* (Ref. 9) and Jensen *et al.* (Ref. 11). Curves are explained in the text.

et al. high-carrier-concentration datum in the previous paragraph.) For no reasonable set of Q values we can get distortions are large as those reported by Schilz. It might be argued that Schilz's data may be internally consistent in the sense that the large nonellipsoidal distortions imply very large Q's which in turn are consistent with the very large K's apparent in Fig. 14 (see the discussion in Sec. III A). However, the Schilz data as a whole seem so inconsistent with all the other PbTe data that we are inclined to discount their reliability. We conclude, therefore, that nonellipsoidal distortions of the Fermi surface in PbTe clearly exist but are relatively small at all carrier concentrations and Fermi energies so far studied.

IV. CONCLUSIONS

We have applied the multiband model electron dispersion relation given by Eq. (1) to an analysis of the available experimental data for PbTe. We find that it provides a useful tool with which to examine the consistency (or lack of consistency) of the whole body of data. The principal conclusions which result from our analysis are: (a) The transverse-conduction-band-edge effective mass is almost certainly significantly smaller than the commonly used value derived from the early experiments of Cuff *et al.* (b) The conduction- and valence-band mass anisotropy ratios vary with Fermi energy or carrier concentration, but only weakly in the range of carrier concentrations so far investigated ($\lesssim 5\times 10^{19}$ cm^{-3}). This conclusion is in substantial disagreement with most of the earlier data for p-PbTe, but agrees with more recent data. (c) Both the conduction and valence bands are strongly nonparabolic but only weakly nonellipsoidal for carrier concentrations less than about 5×10^{19} cm^{-3}. (d) The deviation from "mirror symmetry" of the conduction and valence bands is significant. (e) The neglect of nonellipsoidal distortions of the Fermi surface is often justified, but the analysis of experimental data using an ellipsoidal nonparabolic model less general than the ellipsoidal truncation of the multiband model (e.g., the Kane or simplified Cohen models) is likely to yield misleading results. (f) Existing theoretical calculations of the far-band contributions to the conduction- and valence-band-edge effective masses are not in very good agreement with experiment, especially the transverse contributions.

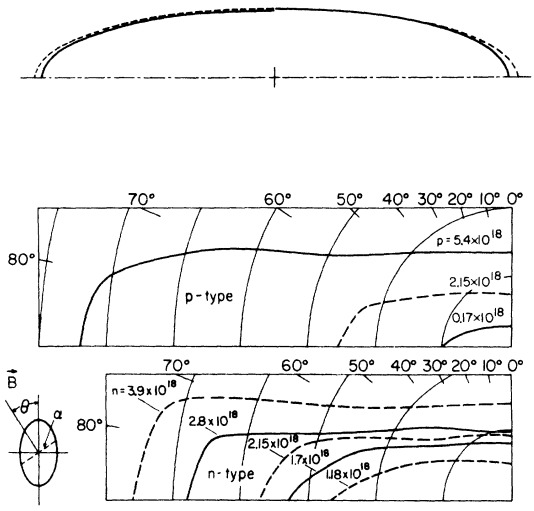

FIG. 14. Angular variation of the de Haas–van Alphen frequency, below as observed by Schilz (Ref. 26) and above as calculated from the multiband model as discussed in the text.

ACKNOWLEDGMENTS

We thank J. R. Burke for providing experimental data prior to publication.

APPENDIX: CALCULATION OF EXPERIMENTAL QUANTITIES WITHIN THE MULTIBAND MODEL

We begin with the MBM dispersion relation, Eq. (3),

$$E\left(1+\frac{E}{E_g}\right)=\frac{p_1^2}{2m_1}\left(1+\frac{E}{E_g}\Delta_1\right)+\frac{p_3^2}{2m_3}\left(1+\frac{E}{E_g}\Delta_3\right)+\frac{p_1^4}{4m_1^2E_g}Q_1+\frac{p_1^2p_3^2}{4m_1m_3E_g}Q_2+\frac{p_3^4}{4m_3^2E_g}Q_3\,. \tag{A1}$$

We have dropped the c or v subscripts for convenience. In calculating the Fermi-surface geometrical quantities we shall need, it is useful to rescale the momentum coordinates of a given constant-energy surface according to the prescription

$$p_\perp=r\left(\frac{2\epsilon(1+\epsilon)m_1E_g}{1+\epsilon\Delta_1}\right)^{1/2}\equiv rS_1(\epsilon)\,,\quad p_3=z\left(\frac{2\epsilon(1+\epsilon)m_3E_g}{1+\epsilon\Delta_3}\right)^{1/2}\equiv zS_3(\epsilon)\,, \tag{A2}$$

where $\epsilon\equiv E/E_g$. Equation (A1) can then be written in the form

$$1=r^2+z^2+R_1r^4+R_2r^2z^2+R_3z^4\,, \tag{A3}$$

where

$$R_1 = \frac{\epsilon(1+\epsilon)}{(1+\epsilon\Delta_1)^2} Q_1, \quad R_2 = \frac{\epsilon(1+\epsilon)}{(1+\epsilon\Delta_1)(1+\epsilon\Delta_3)} Q_2, \quad R_3 = \frac{\epsilon(1+\epsilon)}{(1+\epsilon\Delta_3)^2} Q_3. \tag{A4}$$

This scaling transforms the ellipsoid given by Eq. (A1) with $Q_1 = Q_2 = Q_3 = 0$ into the unit sphere in r-z space. It is important to note that the scaling factors $S_1(\epsilon)$ and $S_3(\epsilon)$ are energy dependent.

We now proceed to calculate de Haas–van Alphen frequencies and cyclotron effective masses.

A. De Haas-van Alphen frequency

The de Haas–van Alphen frequency F is given in general by $F = (c/eh)A_p$, where A_p is an extremal cross-section area of the Fermi surface in a plane normal to the magnetic field. (We use cgs units: F is in Gauss.) We assume that the parameter magnitudes of our model are such that the Fermi surface described by Eq. (A1) resembles a distorted ellipsoid and not, for example, a dumbbell. Then the appropriate cross section is the central one. Suppose the magnetic field is at an angle θ with respect to the p_3 axis. For convenience we assume it to lie in the p_1-p_3 plane. It is easy to show that the central plane normal to the magnetic field in p space transforms into a central plane in r-z space with normal in the x-z plane ($r^2 = x^2 + y^2$) and at an angle ψ with respect to the z axis, where

$$\tan\psi = (S_1/S_3)\tan\theta. \tag{A5}$$

Furthermore, the central cross-section area A_{rz} of the rescaled Fermi surface is related to A_p by

$$\frac{A_p}{A_{rz}} = \frac{S_1^2 S_3}{(S_1^2 \sin^2\theta + S_3^2 \cos^2\theta)^{1/2}}. \tag{A6}$$

To calculate A_{rz}, we first express the intersection of the Fermi surface with the central plane in r-z space in terms of polar coordinates (ρ, φ) in the plane. Then A_{rz} is given simply by

$$A_{rz} = \frac{1}{2}\int_0^{2\pi} \rho^2 \, d\varphi. \tag{A7}$$

Substitution of

$$x = \rho\cos\varphi\cos\psi; \quad y = \rho\sin\varphi; \quad z = -\rho\cos\varphi\sin\psi, \tag{A8}$$

into Eq. (A3) yields

$$1 = \rho^2 + D\rho^4, \quad D = R_1(\cos^2\varphi\cos^2\psi + \sin^2\varphi)^2 + R_2(\cos^2\varphi\cos^2\psi + \sin^2\varphi)\cos^2\varphi\sin^2\psi + R_3\cos^4\varphi\sin^4\psi. \tag{A9}$$

It is easy enough to solve this for ρ^2, but the exact evaluation of the subsequent angular integral, Eq. (A7), is beyond us. However, since we expect (and find) the Q's and, for all Fermi energies of interest, the R's to be small compared with unity, we may expand ρ^2 in a series in the R's and integrate term-by-term. For present purposes it suffices to retain terms only to first order in the R's and thus to take into account the quartic terms in the dispersion relation only to first order in the Q's. To this order, the solution of Eq. (A9) is simply $\rho^2 = 1 - D$. Integration over φ and elimination of ψ in favor of θ yields

$$A_{rz} = \pi(1 - U),$$

$$8U(S_1^2\sin^2\theta + S_3^2\cos^2\theta)^2 = R_1(3S_1^4\sin^4\theta + 8S_1^2S_3^2\sin^2\theta\cos^2\theta + 8S_3^4\cos^4\theta)$$

$$+ R_2(S_1^4\sin^4\theta + 4S_1^2S_3^2\sin^2\theta\cos^2\theta) + R_3(3S_1^4\sin^4\theta). \tag{A10}$$

Using Eq. (A6), we find

$$F = F_0\epsilon_F(1+\epsilon_F)\left(\frac{m_1m_3/m_0^2}{(1+\epsilon_F\Delta_1)(1+\epsilon_F\Delta_3)(\sin^2\theta + \kappa_F\cos^2\theta)}\right)^{1/2}(1-U), \tag{A11}$$

$$U = \frac{\epsilon_F(1+\epsilon_F)}{8(\sin^2\theta + \kappa_F\cos^2\theta)^2}\left(\frac{Q_1}{(1+\epsilon_F\Delta_1)^2}(3\sin^4\theta + 8\kappa_F\sin^2\theta\cos^2\theta + 8\kappa_F^2\cos^4\theta)\right.$$

$$\left. + \frac{Q_2}{(1+\epsilon_F\Delta_1)(1+\epsilon_F\Delta_3)}(\sin^4\theta + 4\kappa_F\sin^2\theta\cos^2\theta) + \frac{Q_3}{(1+\epsilon_F\Delta_3)^2}(3\sin^4\theta)\right). \tag{A12}$$

Here $F_0 = m_0cE_g/e\hbar$ and $\kappa_F = \kappa(\epsilon_F)$, where

$$\kappa(\epsilon)=\frac{m_3}{m_1}\,\frac{1+\epsilon\Delta_1}{1+\epsilon\Delta_3}.$$

The maximum ($\theta=\frac{1}{2}\pi$) and minimum ($\theta=0$) de Haas–van Alphen frequencies are of particular interest. They are

$$F_{\max}=F_0\left(\frac{m_1m_3}{m_0^2}\right)^{1/2}\frac{\epsilon_F(1+\epsilon_F)}{(1+\epsilon_F\Delta_1)^{1/2}(1+\epsilon_F\Delta_3)^{1/2}}(1-U_{\max}),$$

$$U_{\max}=\frac{\epsilon_F(1+\epsilon_F)}{8}\left(\frac{3Q_1}{(1+\epsilon_F\Delta_1)^2}+\frac{Q_2}{(1+\epsilon_F\Delta_1)(1+\epsilon_F\Delta_3)}+\frac{3Q_3}{(1+\epsilon_F\Delta_3)^2}\right), \tag{A13}$$

and

$$F_{\min}=F_0\frac{m_1}{m_0}\,\frac{\epsilon_F(1+\epsilon_F)}{1+\epsilon_F\Delta_1}(1-U_{\min}),\quad U_{\min}=\frac{\epsilon_F(1+\epsilon_F)Q_1}{(1+\epsilon_F\Delta_1)^2}. \tag{A14}$$

For $\theta=0$, the central Fermi-surface cross section is circular and its area and hence $F_{\min}$ can be calculated exactly without resorting to the approximation which led to Eq. (A14). This exact result is

$$F_{\min}=F_0\frac{m_1}{m_0}\,(2Q_1)^{-1}\{-(1+\epsilon_F\Delta_1)+[(1+\epsilon_F\Delta_1)^2+4Q_1\epsilon_F(1+\epsilon_F)]^{1/2}\}. \tag{A15}$$

B. Cyclotron effective mass

The cyclotron effective mass corresponding to an orbit bounding a p-space cross section area A_p is in general given by $(2\pi)^{-1}\partial A_p/\partial E$. The normalized (to the free electron mass) cyclotron mass corresponding to the extremal Fermi surface cross section is thus

$$\mu=\frac{1}{2\pi m_0}\left.\frac{\partial A_p}{\partial E}\right|_{E=E_F}=\frac{1}{2\pi m_0E_g}\left.\frac{\partial A_p}{\partial\epsilon}\right|_{\epsilon=\epsilon_F}. \tag{A16}$$

Performing the indicated differentiation for the extremal A_p calculated in the previous section, we find

$$\mu=\frac{(m_1m_3/m_0^2)^{1/2}[G(\frac{1}{2},\frac{1}{2})\sin^2\theta+\kappa_FG(1,0)\cos^2\theta]}{(1+\epsilon_F\Delta_1)^{1/2}(1+\epsilon_F\Delta_3)^{1/2}(\sin^2\theta+\kappa_F\cos^2\theta)^{3/2}}\,(1-V), \tag{A17}$$

$$\begin{aligned}V=&\frac{\epsilon_F(1+\epsilon_F)}{4(\sin^2\theta+\kappa_F\cos^2\theta)^2[G(\frac{1}{2},\frac{1}{2})\sin^2\theta+\kappa_FG(1,0)\cos^2\theta]}\\&\times\left(\frac{Q_1}{(1+\epsilon_F\Delta_1)^2}\{3\sin^4\theta[G(\tfrac{5}{4},\tfrac{1}{4})\sin^2\theta+\kappa_FG(\tfrac{5}{2},-1)\cos^2\theta]\right.\\&\quad+8\kappa_F\sin^2\theta\cos^2\theta[G(\tfrac{3}{4},\tfrac{3}{4})\sin^2\theta+\kappa_FG(2,-\tfrac{1}{2})\cos^2\theta]+8\kappa_F^2\cos^4\theta[G(\tfrac{1}{4},\tfrac{5}{4})\sin^2\theta+\kappa_FG(\tfrac{3}{2},0)\cos^2\theta]\}\\&+\frac{Q_2}{(1+\epsilon_F\Delta_1)(1+\epsilon_F\Delta_3)}\{\sin^4\theta[G(\tfrac{3}{4},\tfrac{3}{4})\sin^2\theta+\kappa_FG(2,-\tfrac{1}{2})\cos^2\theta]\\&\quad+4\kappa_F\sin^2\theta\cos^2\theta[G(\tfrac{1}{4},\tfrac{5}{4})\sin^2\theta+\kappa_FG(\tfrac{3}{2},0)\cos^2\theta]\}\\&\left.+\frac{Q_3}{1+\epsilon_F\Delta_3}\{3\sin^4\theta[G(\tfrac{1}{4},\tfrac{5}{4})\sin^2\theta+\kappa_FG(\tfrac{3}{2},0)\cos^2\theta]\}\right),\end{aligned}$$

where

$$G(a,b)\equiv1+2\epsilon_F-\epsilon_F(1+\epsilon_F)[a\Delta_1/(1+\epsilon_F\Delta_1)+b\Delta_3/(1+\epsilon_F\Delta_3)].$$

The maximum ($\theta=\frac{1}{2}\pi$) and minimum ($\theta=0$) cyclotron masses are

$$\mu_{\max}=\left(\frac{m_1m_3}{m_0^2}\right)^{1/2}\frac{G(\frac{1}{2},\frac{1}{2})}{(1+\epsilon_F\Delta_1)^{1/2}(1+\epsilon_F\Delta_3)^{1/2}}\,(1-V_{\max}), \tag{A18}$$

$$V_{\max}=\frac{\epsilon_F(1+\epsilon_F)}{4G(\frac{1}{2},\frac{1}{2})}\left(\frac{3Q_1G(\frac{5}{4},\frac{1}{4})}{(1+\epsilon_F\Delta_1)^2}+\frac{Q_2G(\frac{3}{4},\frac{3}{4})}{(1+\epsilon_F\Delta_1)(1+\epsilon_F\Delta_3)}+\frac{3Q_3G(\frac{1}{4},\frac{5}{4})}{(1+\epsilon_F\Delta_3)^2}\right),$$

$$\mu_{\min}=\frac{m_1}{m_0}\,\frac{G(1,0)}{1+\epsilon_F\Delta_1}\,(1-V_{\min}),\quad V_{\min}=\frac{2\epsilon_F(1+\epsilon_F)G(\frac{3}{2},0)Q_1}{(1+\epsilon_F\Delta_1)^2G(1,0)}. \tag{A19}$$

An exact expression for $\mu_{\min}$ can be obtained by differentiation of the A_p which leads to Eq. (A15). The result is

$$\mu_{\min}=\frac{m_1}{m_0}(2Q_1)^{-1}\left(-\Delta_1+\frac{\Delta_1(1+\epsilon_F\Delta_1)+2Q_1(1+2\epsilon_F)}{[(1+\epsilon_F\Delta_1)^2+4Q_1\epsilon_F(1+\epsilon_F)]^{1/2}}\right). \tag{A20}$$

Note that, because of the energy dependence of the scaling factors S_1 and S_3, the angular variation of the cyclotron mass for the ellipsoidal-nonparabolic version of the MBM dispersion relation obtained by setting the Q's equal to zero differs from the usual angular variation for an ellipsoidal-parabolic model.

C. Mass anisotropy ratios

A parameter often used to characterize a spheroidal constant-energy surface is the mass-anisotropy ratio K, defined as the ratio of the longitudinal to transverse effective mass. It is also commonly used for nonparabolic nonellipsoidal bands of the type we are considering here. However, some care is then required in its definition. The longitudinal and transverse masses at the Fermi surface are not separately experimentally accessible. One can, however, define two different "mass-anisotropy ratios" in terms of quantities which *are* directly accessible experimentally. They are (a) the quantum oscillation or de Haas–van Alphen mass anisotropy ratio, $K_q\equiv(F_{\max}/F_{\min})^2$, and (b) the cyclotron mass anisotropy ratio, $K_\mu\equiv(\mu_{\max}/\mu_{\min})^2$. Both depend on the Fermi energy and hence the carrier concentration and Fermi energy.

These ratios are easily calculated for the MBM from the preceding results. To first order in the Q's they are

$$\frac{K_q}{K_0}=\frac{1+\epsilon_F\Delta_1}{1+\epsilon_F\Delta_3}(1-W),\quad W=\frac{\epsilon_F(1+\epsilon_F)}{4}\left(\frac{-5Q_1}{(1+\epsilon_F\Delta_1)^2}+\frac{Q_2}{(1+\epsilon_F\Delta_1)(1+\epsilon_F\Delta_3)}+\frac{3Q_3}{(1+\epsilon_F\Delta_3)^2}\right) \tag{A21}$$

and

$$\frac{K_\mu}{K_0}=\frac{1+\epsilon_F\Delta_1}{1+\epsilon_F\Delta_3}\,\frac{G^2(\frac{1}{2},\frac{1}{2})}{G^2(1,0)}\,(1-X), \tag{A22}$$

$$X=\epsilon_F(1+\epsilon_F)\left[\frac{Q_1}{(1+\epsilon_F\Delta_1)^2}\left(\frac{3}{2}\,\frac{G(\frac{5}{4},\frac{1}{4})}{G(\frac{1}{2},\frac{1}{2})}-4\,\frac{G(\frac{3}{2},0)}{G(1,0)}\right)+\frac{Q_2}{(1+\epsilon_F\Delta_1)(1+\epsilon_F\Delta_3)}\,\frac{1}{2}\,\frac{G(\frac{3}{4},\frac{3}{4})}{G(\frac{1}{2},\frac{1}{2})}+\frac{Q_3}{(1+\epsilon_F\Delta_3)^2}\,\frac{3}{2}\,\frac{G(\frac{1}{4},\frac{5}{4})}{G(\frac{1}{2},\frac{1}{2})}\right].$$

Note that the parameter κ_F introduced previously [see Eq. (A12)] is simply K_q for the ellipsoidal-nonparabolic version of the MBM.

D. Carrier concentration

The total carrier concentration is $N=2n\hbar^{-3}\Omega_p$, where n is the total number of "ellipsoids" (four for PbTe) and Ω_p is the volume of a single "ellipsoid" in p space. To calculate the volume Ω_{rz} of a scaled "ellipsoid" in r-z space, we express Eq. (A3) in spherical coordinates, $r=\rho\sin\theta$, $z=\rho\cos\theta$:

$$1=\rho^2+\rho^4(R_1\sin^4\theta+R_2\sin^2\theta\cos^2\theta+R_3\cos^4\theta). \tag{A23}$$

Then

$$\Omega_{rz}=\frac{2\pi}{3}\int_0^{\pi}\rho_F^3\sin\theta\,d\theta. \tag{A24}$$

This integral is easily evaluated to first order in the Q's:

$$\Omega_{rz}=\frac{4\pi}{3}(1-Y),\quad Y=\frac{\epsilon_F(1+\epsilon_F)}{10}\left(\frac{8Q_1}{(1+\epsilon_F\Delta_1)^2}+\frac{2Q_2}{(1+\epsilon_F\Delta_1)(1+\epsilon_F\Delta_3)}+\frac{3Q_3}{(1+\epsilon_F\Delta_3)^2}\right).$$

Using the appropriate scaling factors, Eq. (A2), to find Ω_p, we find

$$N=N_0\,\frac{\epsilon_F^{3/2}(1+\epsilon_F)^{3/2}}{(1+\epsilon_F\Delta_1)(1+\epsilon_F\Delta_3)^{1/2}}\,(1-Y), \tag{A26}$$

where

$$N_0=(8\sqrt{2}/3\pi^2\hbar^3)m_1m_3^{1/2}E_g^{3/2}.$$

E. Series expansions

It is often useful to have series expansions of the quantities we have calculated which are appropriate for small carrier concentration. Suitable expansion parameters are ϵ_F, $(F_{\min} m_0/F_0 m_1)$, $[F_{\max} m_0/F_0(m_1 m_3)^{1/2}]$, and $(N/N_0)^{2/3}$. These four parameters become equal to the limit of small carrier concentration. Of the many possibilities, we list below some used in the discussions of the present paper (in most cases we have dropped terms second order in the Q's to be consistent with the foregoing calculations):

$$\mu_{\min}^2 = \left(\frac{m_1}{m_0}\right)^2 \left[1 + \sum_{n=1}^{\infty} A_n \left(\frac{F_{\min} m_0}{F_0 m_1}\right)^n\right], \quad A_1 = 4(1 - \Delta_1 - Q_1), \quad A_2 = -6(1 - \Delta_1 - Q_1)(\Delta_1 + 2Q_1). \tag{A27}$$

$$\frac{K_q}{K_0} = 1 + \sum_{n=1}^{\infty} B_n \left(\frac{N}{N_0}\right)^{2n/3}, \quad B_1 = (\Delta_1 - \Delta_3) + \tfrac{1}{4}(5Q_1 - Q_2 - 3Q_3),$$

$$B_2 = (\Delta_1 - \Delta_3)[\tfrac{2}{3}(\Delta_1 - \Delta_3) - 1] + \tfrac{1}{60}[Q_1(7\Delta_1 - 82\Delta_3) + Q_2(-2\Delta_1 + 17\Delta_3) + Q_3(-63\Delta_1 + 108\Delta_3)]. \tag{A28}$$

$$\frac{K_\mu}{K_0} = 1 + \sum_{n=1}^{\infty} C_n \left(\frac{N}{N_0}\right)^{2n/3}, \quad C_1 = 2(\Delta_1 - \Delta_3) + \tfrac{1}{2}(5Q_1 - Q_2 - 3Q_3),$$

$$C_2 = (\Delta_1 - \Delta_3)[\tfrac{31}{12}(\Delta_1 - \Delta_3) - 3] + \tfrac{1}{120}[Q_1(223\Delta_1 - 673\Delta_3) + Q_2(-53\Delta_1 + 143\Delta_3) + Q_3(-475\Delta_1 + 702\Delta_3)]. \tag{A29}$$

$$\frac{F_{\min} m_0}{F_0 m_1} = \sum_{n=1}^{\infty} D_n \left(\frac{N}{N_0}\right)^{2n/3}, \quad D_1 = 1, \quad D_2 = -\tfrac{1}{3}(\Delta_1 - \Delta_3) + \tfrac{1}{15}(-7Q_1 + 2Q_2 + 3Q_3). \tag{A30}$$

---

*Research supported by the NSF under Grant No. GP-40376 and by the Advanced Research Projects Agency of the Dept. of Defense as monitored by the Air Force Office of Scientific Research under Contract No. F44620-75-C-0069.

†Present address: Dept. of Electrical Engineering and Science, Moore School, University of Pennsylvania, Philadelphia, Pa. 19104.

[1]R. Dalven, in *Solid State Physics*, edited by H. Ehrenreich, F. Seitz, and D. Turnbull (Academic, New York, 1973), Vol. 28, p. 179.
[2]C. R. Hewes, M. S. Adler, and S. D. Senturia, Phys. Rev. B 7, 5195 (1973).
[3]G. Martinez, M. Schlüter, and M. L. Cohen, Phys. Rev. B 11, 651 (1975).
[4]M. H. Cohen, Phys. Rev. 121, 387 (1961).
[5]J. O. Dimmock, in *The Physics of Semimetals and Narrow-Gap Semiconductors*, edited by D. L. Carter and R. T. Bate (Pergamon, New York, 1971), p. 319.
[6]M. S. Adler, C. R. Hewes, and S. D. Senturia, Phys. Rev. B 7, 5186 (1973).
[7]E. O. Kane, J. Phys. Chem. Solids 1, 249 (1956).
[8]K. F. Cuff, M. R. Ellett, C. D. Kuglin, and L. R. Williams, in *Proceedings of the International Conference on the Physics of Semiconductors, Paris, 1964*, edited by M. Hulin (Academic, New York, 1964), p. 677.
[9]J. R. Burke, B. Houston, and H. T. Savage, Phys. Rev. B 2, 1977 (1970).
[10]T. E. Thompson, P. R. Aron, B. S. Chandrasekhar, and D. N. Langenberg, Phys. Rev. B 4, 518 (1971).
[11]J. D. Jensen, B. Houston, and J. R. Burke (unpublished).
[12]G. M. T. Foley and D. N. Langenberg, preceding paper, Phys. Rev. B 15, 4830 (1977).
[13]R. Nii, J. Phys. Soc. Jpn. 19, 58 (1964); R. Nii and A. Kobayashi, in *Plasma Effects in Solids* (Dunod, Paris, 1964), p. 65; H. Numata and Y. Uemura, J. Phys. Soc. Jpn. 19, 2140 (1964).
[14]S. Perkowitz, Phys. Rev. 182, 828 (1969).
[15]D. L. Mitchell, E. D. Palik, and J. N. Zemel, in Ref. 8, p. 325.
[16]J. F. Butler and A. R. Calawa, in *Physics of Quantum Electronics*, edited by P. L. Kelley, B. Lax, and P. E. Tannenwald (McGraw-Hill, New York, 1965), p. 458.
[17]M. Fujimoto, J. Phys. Soc. Jpn. 21, 1706 (1966).
[18]J. N. Walpole and A. L. McWhorter, Phys. Rev. 158, 708 (1967).
[19]S. G. Bishop and B. W. Henvis, Solid State Commun. 7, 437 (1969).
[20]D. D. Buss and M. A. Kinch, in *Physics of IV-VI Compounds and Alloys*, edited by S. Rabii (Gordon and Breach, New York, 1974), p. 209.
[21]P. J. Lin and L. Kleinman, Phys. Rev. 142, 478 (1966).
[22]S. Rabii, Phys. Rev. 167, 801 (1968).
[23]R. Glosser, J. Kinoshita, and B. Rennex, Phys. Rev. Lett. 33, 1027 (1974).
[24]R. Dalven, Phys. Rev. Lett. 35, 66 (1975).
[25]K. F. Cuff, M. R. Ellett, and C. D. Kuglin, in *Proceedings of the International Conference on the Physics of Semiconductors*, edited by A. C. Strickland (Institute of Physics and Physical Society, London, 1962), p. 316.
[26]W. Schilz, J. Phys. Chem. Solids 30, 903 (1969).
[27]P. J. Stiles, E. Burstein, and D. N. Langenberg, J. Appl. Phys. 32, 2174 (1961).
[28]P. J. Stiles, E. Burstein, and D. N. Langenberg, Phys. Rev. Lett. 9, 257 (1962).
[29]G. Coste, Phys. Status Solidi 20, 361 (1967).